Comparative Study of Vibration on 10-Pole 12-Slot and 14-Pole 12-Slot PMSM Considering Tooth Modulation Effect

Jae-Hyun Kim, Soo-Hwan Park, Jun-Yeol Ryu, and Myung-Seop Lim, *Member, IEEE*

***Abstract*—In this article, the electromagnetic force and vibration characteristics of 10-pole 12-slot and 14-pole 12-slot permanent magnet synchronous motors (PMSMs) are examined considering the tooth modulation effect. In contrast to the conventional electromagnetic force analysis process which considers only the radial force of the lowest spatial harmonic order, the radial and tangential forces include low and high spatial harmonic orders which can be modulated with a lower spatial harmonic order, are analyzed. Then, a structural finite-element (FE) model is developed, and vibration analysis is performed by applying a modulated force and moment. In the analysis, the amplitude and phase of the modulated radial force, tangential force, and moment are considered. The vibration analysis result shows that the 10-pole 12-slot PMSM is disadvantageous with respect to vibration when compared to the 14-pole 12-slot PMSM owing to the large modulated force. Also, it is confirmed that the effect of modulated tangential force and moment cannot be neglected, and the phase difference between modulated radial, tangential force and moment is also an important factor in vibration. Finally, the two motors are fabricated, and the validity of the FE analysis results is verified using the test results.**

***Index Terms*—Electromagnetic force, fractional slot concentrated winding (FSCW) permanent magnet synchronous motor (PMSM), tooth modulation effect, vibration characteristic.**

I. Introduction

PERMANENT magnet synchronous motors (PMSMs) are widely used in many industries due to their high efficiency and power density [1]–[3]. A PMSM is classified into integer slot distributed winding and fractional slot concentrated winding (FSCW) based on the combination of pole and slot numbers [4]. Among them, the FSCW PMSM exhibits high fundamental and low harmonic winding factors, and it exhibits high manufacturability compared to integer slot winding [5]. However, the FSCW generates many electromagnetic force spatial harmonics, which are also termed as vibration orders, due to armature magneto-motive force (MMF) and slotting effect. This leads to a lower vibration order of the electromagnetic force when compared to integer slot winding [6]–[8]. Typically, the vibration characteristics of FSCW are worse than those of integer slot winding because a force with a low vibration order causes a large vibration [9].

Hence, while utilizing the advantages of the FSCW PMSM, many studies are being actively conducted to improve the vibration characteristics of FSCW PMSMs [10]–[12]. It is well known that the lowest vibration order of FSCW is determined by the combination of pole and slot numbers, and the noise and vibration levels are determined by the lowest vibration order [13]. Therefore, many studies have been conducted on the electromagnetic force and vibration based on to the combination of pole and slot numbers [14]–[17]. In [16], according to the combination of pole and slot numbers, radial force and vibration performance of an FSCW PMSM were analyzed. The vibration characteristics were solely predicted based on the amplitude of the radial force of the lowest vibration order, without considering high spatial harmonic order of radial force. Similarly, in [17], noise characteristics were estimated using only the lowest vibration order according to the pole/slot combination. However, recently, the tooth modulation effect has been revealed that when a high vibration order force is applied to the tooth-slot structure, it is modulated to low vibration order [18]. Given that a high vibration order can lead to vibrations that are as high as those of a low vibration order, the vibration level cannot be determined only with the lowest vibration order and its amplitude as in previous studies. As a study related to tooth modulation, a hybrid model for vibration synthesis, considering tangential force, was proposed in [19]. The frequency response function (FRF) and shape function due to a unit concentrated radial force, tangential force and moment were developed, and the effects of the tooth modulation effect and tangential force were analyzed. In [20], the vibration characteristics of an FSCW PMSM with a bread-loaf permanent magnet (PM) were analyzed, and it was revealed that the bread-loaf PM can deteriorate the motor vibration when considering the tooth modulation effect. In [21], the modulation

Manuscript received 14 January 2022; revised 2 May 2022; accepted 29 May 2022. Date of publication 14 June 2022; date of current version 12 December 2022. This work was supported by the National Research Foundation of Korea (NRF) grant funded by the Korea government (MSIT) under Grant NRF-2020R1A4A4079701. *(Corresponding author: Myung-Seop Lim.)*

The authors are with the Department of Automotive Engineering, Hanyang University, Seoul 04763, South Korea (e-mail: zerg1258@hanyang.ac.kr; shwanp14@hanyang.ac.kr; jesus0925@hanyang.ac.kr; myungseop@hanyang.ac.kr).

Color versions of one or more figures in this article are available at https://doi.org/10.1109/TIE.2022.3181418.

Digital Object Identifier 10.1109/TIE.2022.3181418

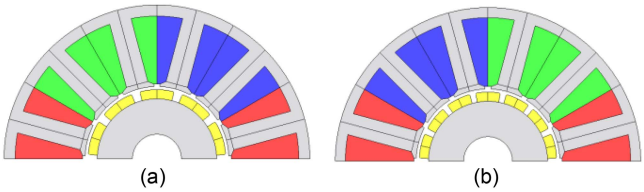

Fig. 1. Configuration of the model. (a) 12s10p. (b) 12s14p.

effect was analytically derived based on the vibration order, number of slots, and slot opening angle.

However, even though the pole and slot number combination significantly affect vibration, there are few studies on vibration considering the tooth modulation effect based on the combination of pole and slot numbers of FSCW PMSM. Therefore, in this article, the vibration characteristics of the 10-pole 12-slot (12s10p) and 14-pole 12-slot (12s14p) were analyzed considering tooth modulation effect. Specifically, the similarity of the air-gap electromagnetic force density (AEFD) of the two models was compared, and the difference in the modulation effect, which led to difference in vibration characteristics was investigated. The armature winding configuration, winding factors, vibration orders of 12s10p and 12s14p FSCW PMSMs are the same. Also, their amplitude of radial and tangential AEFD of lowest vibration order is similar. However, given that they exhibit different numbers of poles, the amplitude of the electromagnetic force for each vibration order differs. For example, in 12s10p, the tenth vibration order is largely generated by the PM MMF at $2f_e$, which is twice the fundamental frequency. However, in 12s14p, the 14th vibration order is largely generated by the PM MMF at $2f_e$. The 10th and 14th vibration orders are both modulated to the same 2nd vibration order by 12 tooth-slot structure. However, the amplitude of the modulated force varies, which can lead to a difference in vibration.

II. Air-Gap Electromagnetic Force Density

In this section, the amplitudes and phases of the radial and tangential electromagnetic force densities are analyzed according to the vibration order of a 12s10p and 12s14p PMSM. For a fair comparison, the two models are designed such that they exhibit the same current density. Furthermore, the tooth and yoke thicknesses of each model were determined to maximize the average torque. The 12s14p PMSM, which has a larger pole number than the 12s10p PMSM, is designed with a thinner yoke thickness. This is structurally disadvantageous with respect to vibration [16]. The configuration and specifications of the motors are presented in Fig. 1 and Table I.

According to the Maxwell stress tensor method, the radial AEFD can be expressed in terms of the radial and tangential air-gap magnetic flux densities, as follows:

$$f_r = \frac{B_r^2 - B_t^2}{2\mu_0} \approx \frac{B_r^2}{2\mu_0} \tag{1}$$

where B_r and B_t are the radial and tangential air-gap magnetic flux density neglecting the slotting effect, respectively, and μ_0 denotes the vacuum permeability. Typically, the radial AEFD

TABLE I
Specifications of 10-Pole 12-Slot and 14-Pole 12-Slot PMSM

Parameter	Unit	Value	
		12s10p	12s14p
Stator outer diameter	mm	100.0	
Rotor outer diameter	mm	45.0	
Stack length	mm	50.0	
Tooth width	mm	7.25	7.0
Yoke width	mm	3.62	3.3
Airgap length	mm	1.0	
Slot opening	mm	2.0	
Number of series turns per phase	-	112	114
PM height	mm	3.0	
Pole arc/pole pitch ratio	-	0.8	
PM remanence	T	1.2	
Current density	A_{rms}/mm^2	5.0	
Rated torque	Nm	3.0	
Rated speed	r/min	1,000	

can be expressed as a radial air-gap magnetic flux density because the tangential air-gap magnetic flux density is very small when compared to the radial air-gap magnetic flux density. The radial air-gap magnetic flux density can be expressed in terms of the PM field, armature reaction, and relative permeance as follows:

$$B_r = (B_{\mathrm{PM}} + B_{\mathrm{arm}})\lambda_s \tag{2}$$

$$B_{\mathrm{PM}} = \sum_{\mu=2k-1} B_\mu \cos(\mu p\theta - \mu\omega t + \beta_\mu) \tag{3}$$

$$B_{\mathrm{arm}} = \sum_n \sum_\nu B_{n\nu} \cos(\nu p\theta - n\omega t + \beta_{n\nu}) \tag{4}$$

$$\lambda_s = \lambda_0 + \sum_k \lambda_{sk} \cos(ks\theta) \tag{5}$$

where B_{PM} and B_{arm} are the radial magnetic flux density caused by PM field and armature reaction, respectively, μ is the spatial harmonic order of PM field, ω is the electrical angular velocity, t is the time, p is the pole-pair, θ is the mechanical angle, β is the phase angle, ν is the spatial harmonic order of armature reaction, λ_s is the relative permeance, s is the slot number, and k is the integer. The spatial harmonic order of the armature reaction is determined according to the pole/slot combination, which can be expressed as follows:

$$q = \frac{s}{2mp} = \frac{b}{c},\ \nu = \frac{6k}{c} + 1 \tag{6}$$

where q is the slot number per phase per pole, m is the number of phases, b and c are relatively prime. By substituting (3)–(5) into (1), the radial AEFD can be derived. The vibration order and frequency of the radial AEFD are summarized in Table II based on their sources. In general, the AEFD has the highest amplitude at twice the fundamental frequency, $2f_e$, which is generated by the synthesis of the fundamental air-gap magnetic flux density. Therefore, the vibration orders of the 12s10p and 12s14p FSCW at $2f_e$ are calculated and given in Table III. Here, the interaction between the armature reaction and stator slotting is excluded because the armature reaction of a PMSM is generally less than 20% of the PM field under the full load condition [13]. The

TABLE II
SOURCE, VIBRATION ORDER, AND FREQUENCY OF RADIAL FORCE

Sources	Vibration order	Frequency
PM field	$(\mu_1 \pm \mu_2)p$	$(\mu_1 \pm \mu_2)f_e$
Armature reaction	$(\nu_1 \pm \nu_2)p$	$(n_1 \pm n_2)f_e$
Interaction of PM field and armature reaction	$(\mu \pm \nu)p$	$(\mu \pm n)f_e$
Interaction of PM field and stator slotting	$(\mu_1 \pm \mu_2)p \pm ks$	$(\mu_1 \pm \mu_2)f_e$
Interaction of armature reaction and stator slotting	$(\nu_1 \pm \nu_2)p \pm ks$	$(n_1 \pm n_2)f_e$
Interaction of PM field and armature reaction and stator slotting	$(\mu \pm \nu)p \pm ks$	$(\mu \pm n)f_e$

TABLE III
VIBRATION ORDER OF 12S10P AND 12S14P AT TWICE THE FUNDAMENTAL FREQUENCY

Sources	Vibration order		Frequency
	12s10p	12s14p	
PM field	10 (=2p)	14 (=2p)	$2f_e$
Armature reaction	$10 \pm 6k$	$14 \pm 6k$	$2f_e$
Interaction of PM field and armature reaction	$10 \pm 6k$	$14 \pm 6k$	$2f_e$
Interaction of PM field and stator slotting	$10 \pm 12k$	$14 \pm 12k$	$2f_e$

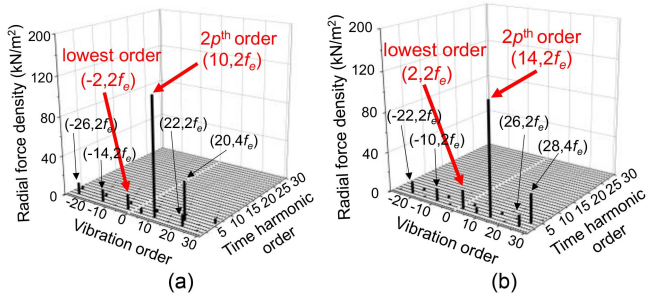

Fig. 2. Radial AEFD spectrum. (a) 12s10p. (b) 12s14p.

vibration orders generated at $2f_e$ by the PM field are 10 (= $2p$) and 14 (= $2p$) in 12s10p and 12s14p PMSM, respectively, and the vibration orders of $\pm 12k$ components are additionally caused by the interaction of the PM field and stator slotting effect. Also, additional vibration orders of $\pm 6k$ components are caused by the armature reaction. Therefore, in 12s10p PMSM, the vibration orders of …, −14, −8, −2, 4, 10, … occur at $2f_e$, and in 12s14p PMSM, the vibration orders of …, −10, −4, 2, 8, 14, … occur at $2f_e$. The vibration orders generated in 12s10p and 12s14p PMSM are the same with exception of their signs. However, it can be predicted that the amplitude of the AEFD of each vibration order is different.

To obtain an accurate radial AEFD, two-dimensional (2-D) electromagnetic FEA is performed at the rated load condition. The 2-D fast Fourier transform (FFT) is performed on the radial AEFD, and the results are shown in Fig. 2. It is confirmed that $10 \pm 12k$ and $14 \pm 12k$, which are vibration orders that can occur due to the PM field and interaction of the PM field and stator slotting, are generated with a large amplitude at $2f_e$. The lowest

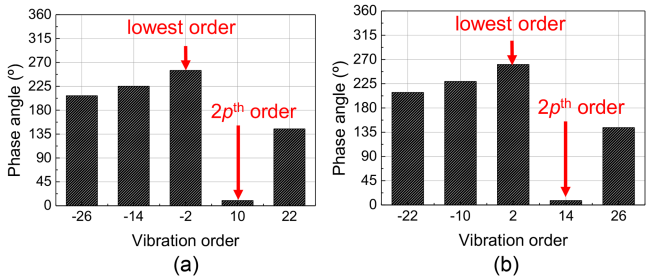

Fig. 3. Phase angle of radial AEFD according to vibration order at $2f_e$. (a) 12s10p. (b) 12s14p.

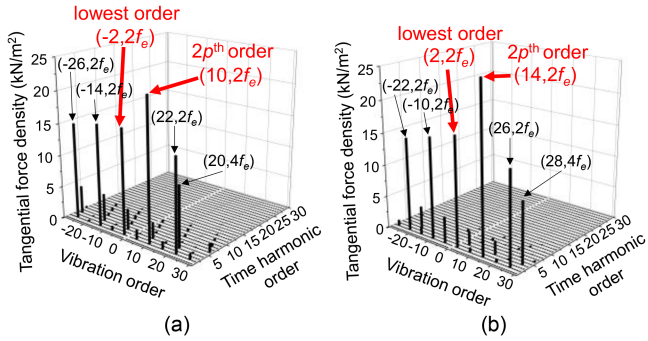

Fig. 4. Tangential AEFD spectrum. (a) 12s10p. (b) 12s14p.

vibration order, which significantly affects the vibration, of the two motors is equal to 2, and the amplitude of the second-order AEFD is also similar. In addition, 2pth order AEFD of the two motors are similar with the exception of their vibration order. Fig. 3 shows the phase angles according to the vibration orders of 12s10p and 12s14p PMSMs at $2f_e$. As shown, the phase angle distributions of the 12s10p and 12s14p PMSMs, including the 2pth order and the lowest order, are similar.

A local tangential force is applied to the edge of the tooth and leads to a lever arm effect, which causes a radial vibration that is as high as the radial force [22]. Also, tangential force can enhance or weaken the radial vibration caused by the radial force [23]. Therefore, it should be considered when analyzing the vibration. According to the Maxwell stress tensor method, the tangential AEFD is expressed in terms of the radial and tangential air-gap magnetic flux densities as follows:

$$f_t = \frac{B_r B_t}{\mu_0}. \tag{7}$$

Since it is difficult to analytically derive the tangential air-gap magnetic flux density, 2-D FEA is performed under the rated load condition to calculate the accurate tangential AEFD. Then, 2-D FFT is performed on the calculated tangential AEFD, and the results are shown in Fig. 4. As shown in the figure, the amplitude of the tangential AEFD is low when compared to the radial AEFD. However, the generated vibration order is the same as that of radial force. Additionally, similar to the radial AEFD, the amplitudes of the lowest and 2pth order tangential AEFD of 12s10p and 12s14p are almost the same. Fig. 5 shows the

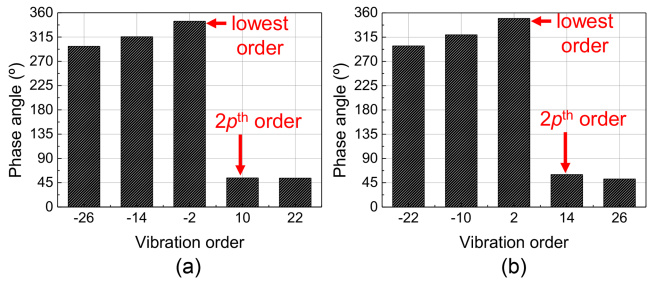

Fig. 5. Phase angle of tangential AEFD according to vibration order at $2f_e$. (a) 12s10p. (b) 12s14p.

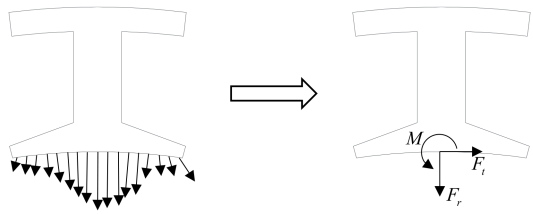

Fig. 6. Distributed electromagnetic force and equivalent concentrated radial and tangential force and moment.

phase angles for each vibration order of the tangential AEFD, which shows the phase angle distributions of 12s10p and 12s14p PMSMs are similar.

Based on the conventional displacement equation assuming the shape of the stator as a cylinder model, the displacement is inversely proportional to the fourth power of the vibration order as follows:

$$Y(v \geq 2) = \frac{12R_{\text{in}}R_{\text{yoke}}^3}{Et_{\text{yoke}}^3(r^2-1)^2} f_r, \ (|r| = v) \tag{8}$$

where Y is the displacement, R_{in} is the stator inner radius, R_{yoke} is the average yoke radius, v is the vibration mode number, t_{yoke} is the yoke width, and E is the elastic modulus of the equivalent ring model. The lowest vibration orders of the radial and tangential AEFDs of the 12s10p and 12s14p PMSMs are both 2, and the amplitudes of the second vibration order force of the two motors are similar. Therefore, it can be expected that the vibration characteristics of the two motors are similar, or the vibration characteristics of 12s14p with a thinner yoke width will be disadvantageous. However, considering the tooth and slot structure of the stator, the force of the higher vibration order is modulated to a lower vibration order [18]. Therefore, it is necessary to analyze the radial and tangential forces by considering the modulation effect.

III. Tooth Modulation Effect

A. Stator Tooth Modulation Effect

In this section, the tooth modulation effects of the radial and tangential AEFDs were analyzed according to the vibration order. As shown in Fig. 6, the AEFD can be equalized to the concentrated radial force, tangential force, and moment. The concentrated force and moment can be expressed as (9)–(11) as

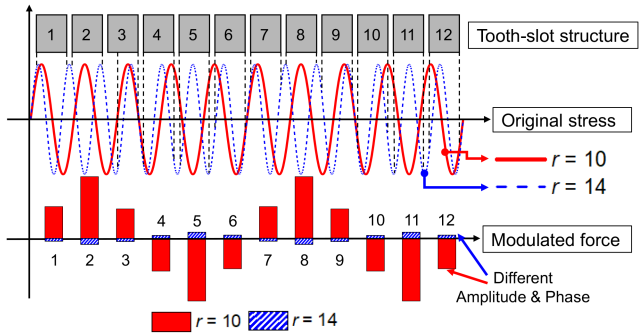

Fig. 7. Tooth modulation effect of 10th and 14th order radial force due to the 12 tooth-slot structure.

the integration of the force acting on the tooth tip

$$F_{r,z} = \int_{\theta_z-\pi/s+\alpha/2}^{\theta_z+\pi/s-\alpha/2} R_{\text{in}}L_{\text{stk}}\{f_r\cos(\theta_z-\theta) + f_t\sin(\theta_z-\theta)\}\,d\theta \tag{9}$$

$$F_{t,z} = \int_{\theta_z-\pi/s+\alpha/2}^{\theta_z+\pi/s-\alpha/2} R_{\text{in}}L_{\text{stk}}\{f_t\cos(\theta_z-\theta) + f_r\sin(\theta_z-\theta)\}\,d\theta \tag{10}$$

$$M_z = \int_{\theta_z-\pi/s+\alpha/2}^{\theta_z+\pi/s-\alpha/2} R_{\text{in}}^2L_{\text{stk}}f_r\sin(\theta_z-\theta)d\theta. \tag{11}$$

Here, F and M are the concentrated force and moment, respectively, f is the distributed AEFD, L_{stk} is the stack length, θ is the mechanical angle, θ_z is the mechanical angle of the zth tooth center, α is the slot opening angle, subscripts r and t denote radial and tangential directions, respectively, and z is the tooth number. Here, the moment term caused by the tangential AEFD is ignored. The vibration order of the radial and tangential AEFDs is determined by the pole and slot number combination as explained in Section II, and the amplitude and phase can be changed according to the PM field, armature reaction, and magnetic saturation. By substituting (1) and (7) into (9)–(11), the concentrated force and moment for each tooth can be calculated. According to the Nyquist–Shannon sampling theory, if the sampling frequency is lower than twice the signal frequency, then the signal appears distorted [20]. A similar phenomenon occurs in the electromagnetic force and stator tooth/slot structure. For example, as shown in Fig. 7, the 10th and 14th order radial AEFD can be modulated to the 2nd order modulated force by the 12-teeth-slots structure of the stator. However, even though 10th and 14th order AEFDs are both modulated to 2nd order modulated force, the amplitude and phase of the modulated force differ according to the original vibration order. If the vibration order of the AEFD is greater than half of the slot number, abs(r) $> s/2$, then the AEFD is modulated to a low vibration order as follows:

$$f^r = f^{r'}\cos[(|r|-ks)\theta + \omega^r t + \beta^r] \tag{12}$$

where superscript r denotes the vibration order, k is the integer, and $f^{r'}$ denotes the modulated force density.

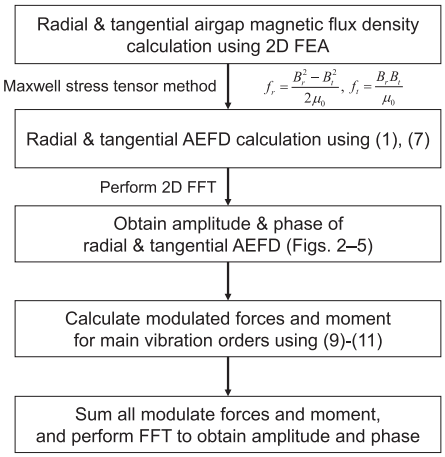

Fig. 8. Calculation process of total modulated force and moment.

B. Comparison of Modulated Forces and Moment of 12s10p and 12s14p PMSM

The modulated forces and moments are calculated and compared in this section. In 12s10p and 12s14p PMSMs, the vibration orders of $2p \pm 6k$ occur, and according to (12), all of them are modulated to the 4th vibration order with the exception of the $2p \pm 12k$. The other vibration orders are modulated to the 2nd vibration order. Given that the displacement by second-order modulated force is much more dominant than the fourth or higher order modulated forces, only the AEFD that modulates the second vibration order is considered, and the other vibration orders are ignored.

Fig. 8 shows the calculation process of the modulated radial force, tangential force and moment from the AEFD. First, the amplitude and phase of the radial and tangential AEFD are calculated using the Maxwell stress tensor method, as shown in Figs. 2–5, which was explained in Section II. Then, the modulated forces are calculated using (9)–(11) for the vibration orders that can modulate into the lowest vibration order, which are … −26, −14, −2, 10, 22, … for 12s10p PMSM. Although the original AEFDs are high order, they are modulated into the lowest vibration order, which correspond to second order. Therefore, the total second-order modulated force can be calculated by summing all of the second-order modulated forces. Finally, by performing FFT of the total modulated forces, the amplitude and phase of the lowest vibration order modulated force can be obtained.

Based on the aforementioned calculation process, the amplitude and phase of the modulated forces and moment under the rated load condition are calculated as shown in Fig. 9. In general, since the amplitude of the AEFD decreases as the vibration order increases, the vibration orders above the 30th were neglected. As shown in Fig. 9, the modulated radial force and moment of 12s14p PMSM are lower than those of 12s10p PMSM even though the amplitudes of the lowest and 2*p*th order AEFD of 12s10p and 12s14p PMSMs calculated in Section II (see Figs. 2 and 4) are similar. Although 10th and 14th vibration orders, which are of the 2*p*th order of 12s10p and 12s14p PMSMs,

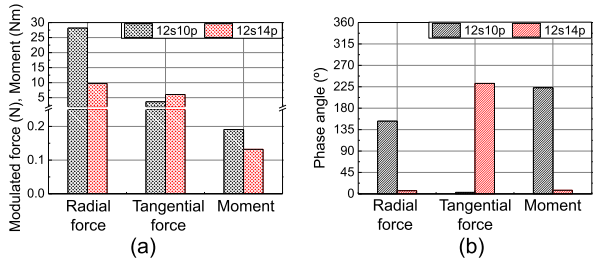

Fig. 9. Amplitude and phase of total modulated 2nd order force at $2f_e$. (a) Amplitude. (b) Phase.

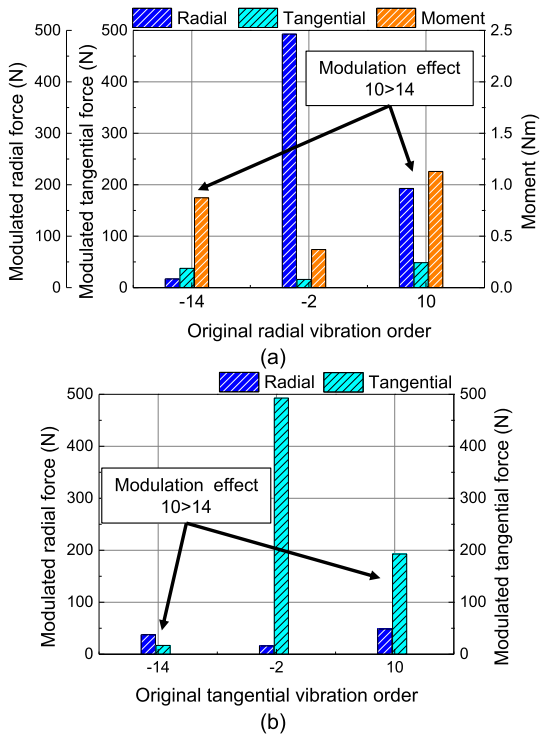

Fig. 10. Amplitude of modulated forces and moment caused by 1 MPa AEFD for vibration orders which modulate to second order. (a) Radial AEFD. (b) Tangential AEFD.

are modulated to the second vibration order by 12 slots, their modulation amplitudes are different owing to their different vibration orders.

To analyze the modulation effect, the modulated force is calculated according to the vibration order when an AEFD of 1 MPa is applied to the 12 stator slots. Fig. 10 shows the amplitude of the modulated radial force, tangential force, and moment according to the vibration order. The modulated radial and tangential forces and moments are generated by the distributed radial AEFD, and the modulated radial and tangential force is generated by the distributed tangential AEFD. As shown, the amplitude of the modulated force and moment differs significantly based on the original vibration order even though the amplitude of the distributed AEFD corresponds to 1 MPa. When comparing the 10th and 14th original vibration orders, the amplitude of the 10th order when compared to that of the 14th order is much higher in terms of the modulated radial and tangential forces,

TABLE IV
AMPLITUDE AND RADIAL VIBRATION CONTRIBUTING PHASE OF TOTAL MODULATED SECOND-ORDER FORCE

Model	Force	Amplitude	Phase	Radial displacement contributing phase
12s10p	Radial	28.1 N	152.7°	152.7°
	Tangential	3.6 N	3.1°	273.1°
	Moment	0.19 Nm	222.7°	312.7°
12s14p	Radial	9.7 N	6.5°	6.5°
	Tangential	6.1 N	232.1°	142.1°
	Moment	0.13 Nm	7.6°	97.6°

and moment. Given that the amplitude of 2pth order radial and tangential AEFD is very high when compared to those of the other vibration orders, the difference in the modulation amplitude of the 10th and 14th orders can lead to a difference corresponding to second-order total modulated force, as shown in Fig. 9.

Although the amplitude of the modulated force and moment of 12s14p PMSM is lower than that of 12s10p PMSM, it is necessary to consider the amplitude and phase of the modulated forces. Fig. 9(b) shows the phase of the total modulated second-order force. In Figs. 3 and 5 of Section II, the phases of the 12s10p and 12s14p PMSMs are similar, but it is confirmed that the phases of the total modulated second-order force significantly differ from each other because the modulation effect varies according to the vibration order. It should be noted that the radial deformation and radial force are in the same phase, while tangential force and moment delays/leads by 90°, respectively, at frequencies below the natural frequency [19]. Therefore, considering the aforementioned phase relationship between the force and radial displacement, the phase contribution to the radial displacement of each total modulated second-order force is calculated and summarized in Table IV. Here, it was assumed that the deformation by the modulated second-order force becomes a pure second mode. For 12s10p PMSM, the radial displacement contribution phase of modulated tangential force and moment are almost the same, whereas the modulated radial force is almost opposite. This indicates that the vibration caused by modulated radial force can be suppressed by modulated tangential force and moment. For 12s14p PMSM, similarly, the radial displacement contributing phase of modulated tangential force and moment are similar, and that of modulated radial force differ by more than 90°. Since the radial displacement contributing phase by the modulated radial force and the tangential force is greater than 90°, the vibration caused by the two forces could cancel each other out. The difference between 12s10p PMSM and 12s14p PMSM is that the modulated radial force of 12s14p PMSM is much smaller compared to 12s10p PMSM due to the modulation effect. In the next section, vibration analysis is performed to compare the vibration characteristics of the 12s10p and 12s14p PMSMs.

IV. VIBRATION ANALYSIS CONSIDERING MODULATION EFFECT

In the previous section, the modulated radial and tangential forces, and moments of 12s10p and 12s14p PMSMs are calculated based on the AEFD. In this section, the vibration characteristics of the two models are calculated and compared using 3-D structural FEA.

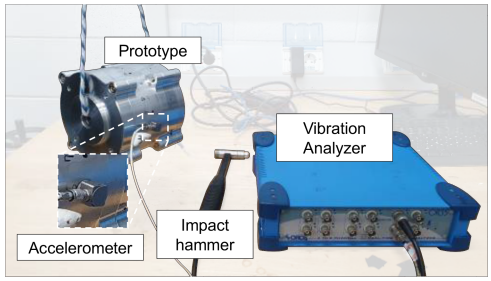

Fig. 11. Modal test setup.

TABLE V
EQUIVALENT MATERIAL PROPERTIES

Items		Stator core	Winding	Housing
Density (kg/m^3)	-	7700	8930	2700
Young's modulus (GPa)	E_x	180		
	E_y	180	1	68.9
	E_z	76.1		
Poisson's ratio	u_{xy}	0.3		
	u_{yz}	0.3	0.1	0.33
	u_{xz}	0.3		
Shear modulus (GPa)	G_{xy}	50		
	G_{yz}	3.8	0.4	25.9
	G_{xz}	3.8		

A. Modal Analysis

Before conducting vibration analysis of the motor by applying electromagnetic force, modal test and modal analysis were performed to build an accurate structural model. Since it is complicated to consider the laminated stator core and winding, the equivalent material properties were obtained from the modal test and parametric fitting, which technique was also adopted in [18], [20]. Fig. 11 shows the modal test setup of 12s10p PMSM prototype. The free boundary condition was realized by hanging the stator assembly without rotor on the elastic rope, and the FRF of a total of 18 points in the circumferential direction of stator assembly was measured. The modal test was conducted using the OROS NVGate data acquisition system, PCB impact hammer 086C03, and the Kistler accelerometer 8776A50. From the modal test, natural frequencies, modal shapes, and damping ratios from the peaks of the FRF were obtained. The equivalent material parameters, which are obtained by parameter fitting using modal test and 3-D structural FEA results using commercial software ANSYS, are given in Table V. The modal test and modal analysis results are given in Table VI. The relative error between measured and simulated results is less than 5.8%, which means that the 3-D structural FEA model is accurate enough. Also, the obtained damping ratio from modal test was applied for the vibration simulation. The 12s10p and 12s14p PMSM have a different stator core configuration and number of turns. Therefore, their equivalent material properties would be different. However, since the two models were designed to

TABLE VI
MODAL TEST AND ANALYSIS RESULTS

Spatial order	Simulated	Measured	Relative error	Damping ratio
2	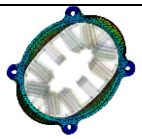 2571 Hz	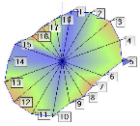 2430 Hz	5.8%	3.06%
3	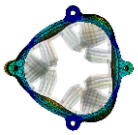 3032 Hz	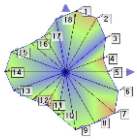 3073 Hz	−1.3%	2.4%
4	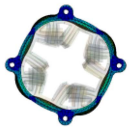 3611 Hz	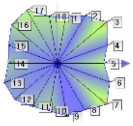 3660 Hz	−1.3%	2.54%

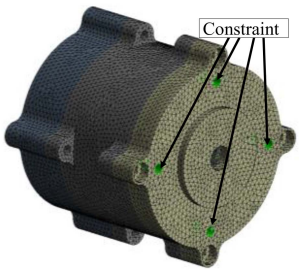

Fig. 12. Configuration of the 3-D structural model with constraint.

compare the effect of different modulated force at $2f_e$, the same equivalent material properties were applied for the two motors.

B. Vibration Analysis Considering Modulated Force

Fig. 12 shows the 3-D structural model using commercial software ANSYS, and for the same conditions as the vibration experiment to be performed later, displacement constraints were applied to the four holes as shown. For the fair comparison, the configuration of enclosure is the same for two motors. Since the lowest order modulated force and moment will cause most of the vibration, vibration analysis was performed by applying only the previously calculated total modulated radial, tangential force, and moment, respectively, at $2f_e$ as shown in Fig. 13. Since $2f_e$ of 12s10p and 12s14p PMSM is 166.6 and 233.3 Hz, respectively, resonance will not occur. As the displacement occurs in the linear region, frequency analysis was performed. Here, the modulated forces and moment are applied on the tooth tip face in a concentrated form. Since the modulated forces and moment have only second spatial harmonic order, which is calculated in Fig. 9, the phase difference of the force for each tooth was set to be 60° to express the second spatial harmonic order.

Fig. 14 shows the vibration analysis results when the total modulated radial, tangential forces and moment are applied,

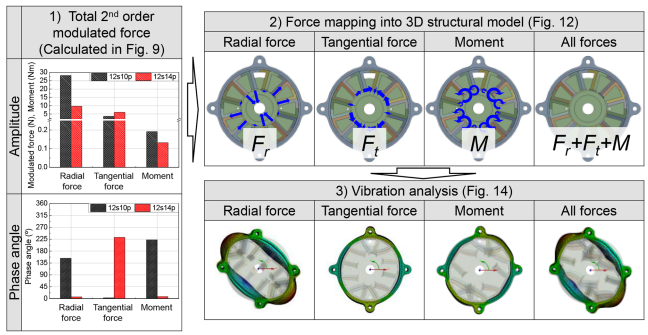

Fig. 13. Vibration analysis process by applying modulated force.

TABLE VII
MAXIMUM RADIAL DISPLACEMENT AT $2F_e$ UNDER RATED LOAD CONDITION

Model	Force	Maximum radial displacement (μm)
12s10p	Radial only	0.348
	Tangential only	0.049
	Moment only	0.075
	All	0.282
12s14p	Radial only	0.110
	Tangential only	0.098
	Moment only	0.048
	All	0.137

respectively. It should be noted that the maximum radial displacement varies according to the phase of the frequency response. Therefore, in Fig. 14, the displacement results in the phase where the maximum displacement occurs, which are 40° and 76° for 12s10p and 12s14p PMSM, respectively, are shown. The maximum radial displacements caused by each modulated force are given in Table VII. Although the 12s14p PMSM is structurally disadvantageous when compared to 12s10p PMSM due to the thinner yoke thickness, the radial displacement of 12s14p PMSM is lower than that of 12s10p PMSM. This is due to the fact that the total modulated force of 12s14p PMSM is lower than that of 12s10p PMSM. Particularly, both motors have the largest radial displacement due to the modulated radial force, and the radial displacement due to modulated radial force of 12s10p PMSM is more than three times larger than 12s14p PMSM. Also, for 12s10p PMSM, the mechanical phases of radial deformation by modulated radial force and radial deformation by modulated tangential force and moment differed by more than 60°. Since the deformation mode is second order, the electrical phase difference is larger than 120°, so the radial vibration by modulated radial force was suppressed by modulated tangential force and moment. However, since the radial displacement caused by the modulated radial force is very large in 12s10p PMSM, the phase of the total deformation is almost the same as the phase when only the modulated radial force is applied. For 12s14p PMSM, like 12s10p PMSM, the phase of radial deformation by modulated radial force and the phase of radial deformation by modulated tangential force and moment are electrically different by larger than 90°. However, because the 12s14p PMSM has very small radial displacement due to small modulated radial force, the phase of total deformation is not the same as that of radial

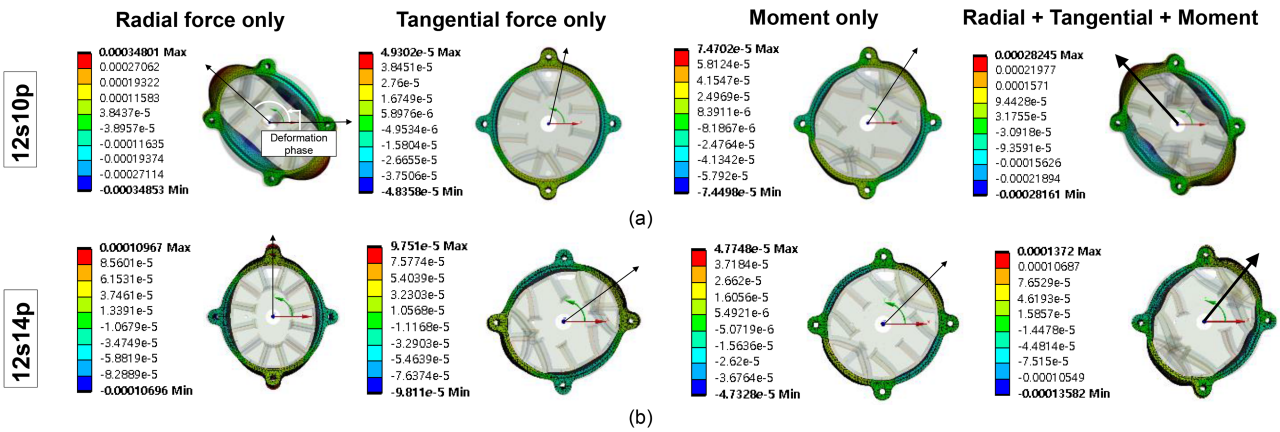

Fig. 14. Radial deformation of 12s10p and 12s14p PMSM caused by total modulated force and moment under rated load condition at $2f_e$. (a) 12s10p. (b) 12s14p.

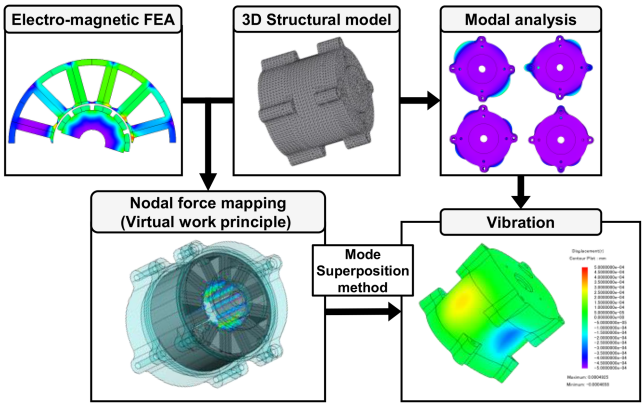

Fig. 15. Vibration calculation procedure by coupled field analysis.

deformation when only modulated radial force is applied, but is similar to that of modulated tangential force and moment. After comprehensively considering all of the aforementioned results, it is confirmed that the radial vibration of 12s14p PMSM is lower than that of the 12s10p PMSM.

C. Vibration Analysis Via Coupled Field FEA

To verify the reliability of the previously performed vibration analysis by applying only modulated forces and moment, an electromagnetic-mechanical coupled field FEA is performed using the commercial software, JMAG. First, to calculate the distributed radial and tangential nodal force of the stator, which is calculated by virtual work principle, a 2-D transient electromagnetic FEA is performed. Then, the calculated force is converted to the frequency domain and projected into the 3-D structural FEA model. In a coupled field FEA, different from vibration analysis done in Section IV-A, forces that include all vibration orders are applied. The process of the coupled field vibration FEA is shown in Fig. 15.

Fig. 16 shows the radial deformation under the rated load condition at $2f_e$, which is calculated via coupled field FEA. The

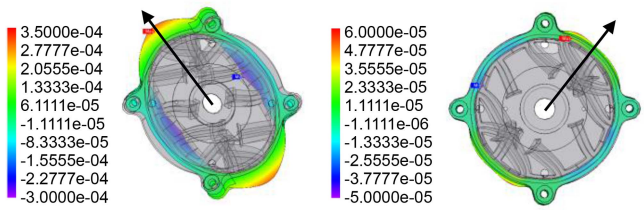

Fig. 16. Total radial deformation by coupled field FEA under rated load condition at $2f_e$. (a) 12s10p. (b) 12s14p.

maximum radial displacements of 12s10p and 12s14p PMSMs are 0.303 and 0.0556 μm, respectively. Although the AEFDs of the two models including the second-order force is almost similar, radial displacement of 12s10p is 5.45 times higher than that of the 12s14p PMSM, due to the different modulation amplitudes of 10th and 14th order AEFD. The deformation configuration and phase of the vibration analysis results shown in Fig. 16, calculated by coupled field FEA, and vibration analysis results shown in Fig. 14 are very similar. Although there is a difference between the maximum radial displacement, it was confirmed that the tendency that the radial displacement of 12s14p PMSM is significantly smaller than that of 12s10p PMSM was consistent. The error between the results can potentially occur because of different force calculation method. The modulated forces are calculated based on AEFD, which is obtained by Maxwell stress tensor method, while nodal forces in coupled field FEA are calculated by virtual work principle. Also, higher harmonics that are not reflected when calculating the modulated force, such as the 38th, 50th, and 62nd order harmonics, may cause errors.

V. Verification

To validate the vibration analysis results, tests of the prototypes of 12s10p and 12s14p PMSMs were performed. Fig. 17 shows the prototype of 12s10p and 12s14p PMSMs. For a fair comparison, the enclosure shapes of the two motors are manufactured as the same, and the rotor and stator shapes are

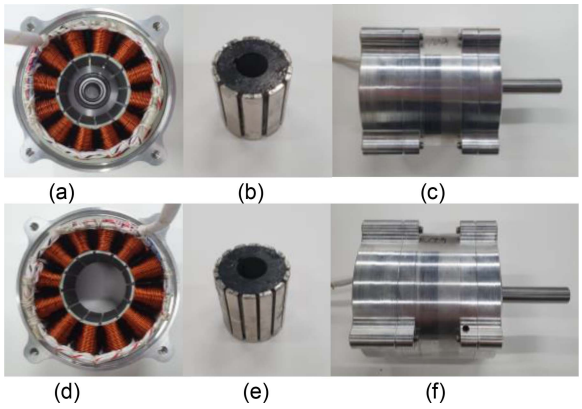

Fig. 17. Prototypes of 12s10p and 12s14p FSCW PMSM. (a) 12s10p stator. (b) 12s10p rotor. (c) 12s10p assembly. (d) 12s14p stator. (e) 12s14p rotor. (f) 12s14p assembly.

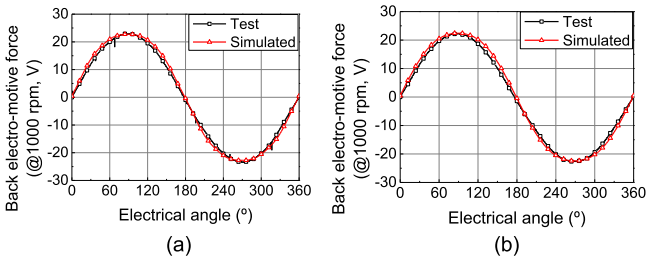

Fig. 18. Test and FEA results of BEMF at 1000 r/min. (a) 12s10p. (b) 12s14p.

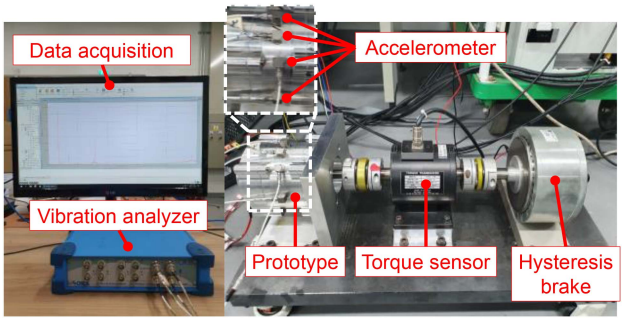

Fig. 19. Vibration test setup.

given in Table I and Fig. 1. To validate whether the prototypes were fabricated correctly, the back electro-motive force (BEMF) was measured, by rotating the prototypes using servo motor at 1000 r/min. Furthermore, the results are compared with the FEA results as shown in Fig. 18. It was confirmed that the test and FEA results are in good agreement.

Fig. 19 shows the vibration test setup, which includes a prototype, torque sensor, hysteresis brake, accelerometer, data acquisition and vibration analyzer. Four accelerometers were attached to the surface of the motor enclosure, two at the center of the tooth and two at the center of the slot. For the accelerometer, Kistler 8776A50 was utilized, which has the acceleration range of 50 g, sensitivity of 100 mV/g. The vibration test was performed using OROS NVGate data acquisition system, under the rated load condition, rotational speed of 1000 r/min and torque

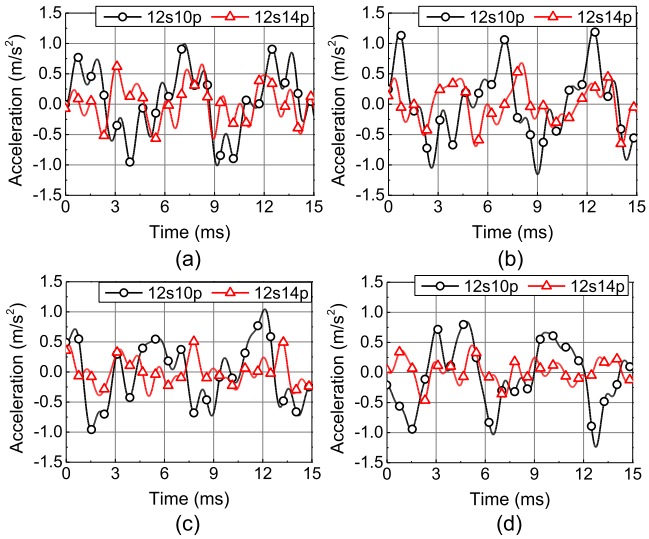

Fig. 20. Time domain vibration waveforms under rated load condition. (a) Sensor 1. (b) Sensor 2. (c) Sensor 3. (d) Sensor 4.

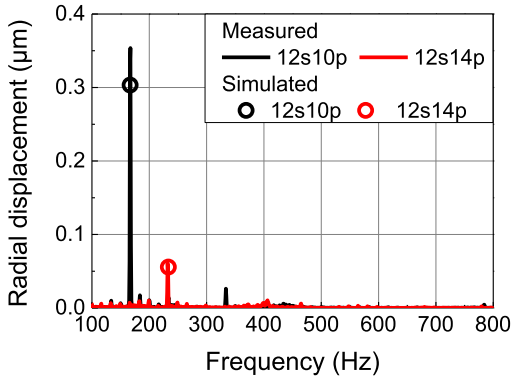

Fig. 21. Vibration test results of 12s10p and 12s14p PMSM under rated load condition in frequency domain.

of 3.0 N·m. The measured accelerations by four accelerometers in time domain are shown in Fig. 20. It should be noted that the vibration waveforms are filtered by a low-pass filter with cutoff frequency of 1500 Hz to highlight the harmonics at $2f_e$. It can be seen that the acceleration of 12s14p in all accelerometers is less than 12s10p PMSM. Then, time domain accelerations were converted into frequency domain to analyze the low-frequency vibration at $2f_e$, and the average acceleration was calculated. To calculate radial displacement, the square of each angular frequency was divided by the acceleration, and the results are shown in Fig. 21. Since the fundamental frequencies of 12s10p and 12s14p PMSM are 166.6 and 233.3 Hz, respectively, the highest displacement occurred at 333.3 and 466.6 Hz, which are twice the fundamental frequency, $2f_e$. As analyzed above, due to the different modulation effect according to the original vibration order, although the amplitude of the lowest vibration order of 12s10p and 12s14p PMSM is similar, it is confirmed that the radial vibration at $2f_e$ was significantly different. The radial displacement at $2f_e$ is 0.354 and 0.0607 μm in 12s10p and 12s14p PMSM, respectively, and 12s10p is about 5.83 times higher than that of 12s14p PMSM.

For 12s10p and 12s14p PMSMs, the test results are higher than the simulation results, which are calculated in Fig. 16 of Section IV-C with coupled field FEA. This error can potentially occur due to the error of modal parameters, such as modal damping, and equivalent material parameters. Also, this can be caused since the structural FE model was built with equivalent parameters without modeling the stacking structure, and rotor. Also, the test system is much more complicated than the structural FEA model due to the torque sensor and hysteresis brake. All these factors can potentially lead to an increase in the motor vibration level in the test when compared to that in the simulation. However, the measured and simulated results confirmed that the radial vibration of 12s14p PMSM is lower than that of the 12s10p PMSM.

VI. Conclusion

In this article, the vibration characteristics considering the tooth modulation effect of 12s10p and 12s14p FSCW PMSMs were investigated. First, the radial and tangential AEFD were analyzed, and the similarities of the AEFD in the two motors were explained. The amplitude and phase of the lowest and pole number vibration order AEFDs of the two motors were almost similar, and the lowest vibration order was also equal to 2. Then, the difference in the tooth modulation effect of the two motors was investigated. Although the lowest vibration order of the two motors was the same, the pole number vibration order ($2p$th) was different. It was revealed that the modulation effects of 10th and 14th order AEFDs are very different, which leads to a difference in the total modulated radial force, tangential force, and moment of the two motors. More specifically, it was confirmed that the 2nd order modulated force and moment generated by the 10th order AEFD are higher than those of the 14th order AEFD. Then, vibration analysis was performed by applying the modulated radial, tangential force, and moment, respectively, and it was confirmed that the vibration of 12s10p PMSM is higher than that of the 12s14p PMSM due to the difference in modulated forces and moments. Finally, the validity of the study was verified through coupled field FEA and a test. It is expected that the analysis of the tooth modulation effect and vibration analysis used in this article can be utilized for other pole and slot number combination PMSMs. However, since the noise performance is dependent on frequency, it cannot be concluded that noise of 12s14p PMSM is more advantageous compared to 12s10p PMSM, and this remains to be further studied.

References

[1] X. Liu, H. Chen, J. Zhao, and A. Belahcen, "Research on the performances and parameters of interior PMSM used for electric vehicles," *IEEE Trans. Ind. Electron.*, vol. 63, no. 6, pp. 3533–3545, Jun. 2016.

[2] P. H. Nguyen, E. Hoang, and M. Gabsi, "Performance synthesis of permanent-magnet synchronous machines during the driving cycle of a hybrid electric vehicle," *IEEE Trans. Veh. Technol.*, vol. 60, no. 5, pp. 1991–1998, Jun. 2011.

[3] K. T. Chau, C. C. Chan, and C. Liu, "Overview of permanent-magnet brushless drives for electric and hybrid electric vehicles," *IEEE Trans. Ind. Electron.*, vol. 55, no. 6, pp. 2246–2257, Jun. 2008.

[4] C. Zhou, X. Huang, Z. Li, and W. Cao, "Design consideration of fractional slot concentrated winding interior permanent magnet synchronous motor for EV and HEV applications," *IEEE Access*, vol. 9, pp. 64116–64126, 2021.

[5] A. S. Abdel-Khalik, S. Ahmed, and A. M. Massoud, "Effect of multilayer windings with different stator winding connections on interior PM machines for EV applications," *IEEE Trans. Magn.*, vol. 52, no. 2, Feb. 2016, Art. no. 8100807.

[6] Z. Wu, Y. Fan, C. H. T. Lee, D. Gao, and K. Yu, "Vibration optimization of FSCW-IPM motor based on iron-core modification for electric vehicles," *IEEE Trans. Veh. Technol.*, vol. 69, no. 12, pp. 14834–14845, Dec. 2020.

[7] T. Sun, J. Kim, G. Lee, J. Hong, and M. Choi, "Effect of pole and slot combination on noise and vibration in permanent magnet synchronous motor," *IEEE Trans. Magn.*, vol. 47, no. 5, pp. 1038–1041, May 2011.

[8] A. M. EL-Refaie, "Fractional-Slot concentrated-windings synchronous permanent magnet machines: Opportunities and challenges," *IEEE Trans. Ind. Electron.*, vol. 57, no. 1, pp. 107–121, Jan. 2010.

[9] J. A. Güemes, A. M. Iraolagoitia, P. Fernández, and M. P. Donsión, "Comparative study of PMSM with integer-slot and fractional-slot windings," in *Proc. 19th Int. Conf. Elect. Machines*, 2010, pp. 1–6.

[10] Z. Wu, Y. Fan, H. Wen, and D. Gao, "Vibration suppression of FSCW-IPM with auxiliary slots," in *Proc. IEEE Energy Convers. Congr. Expo.*, 2018, pp. 3222–3227.

[11] F. Lin, S. G. Zuo, W. Z. Deng, and S. L. Wu, "Reduction of vibration and acoustic noise in permanent magnet synchronous motor by optimizing magnetic forces," *J. Sound Vib.*, vol. 429, 2018. pp. 193–205.

[12] S. Zuo, F. Lin, and X. Wu, "Noise analysis, calculation, and reduction of external rotor permanent-magnet synchronous motor," *IEEE Trans. Ind. Electron.*, vol. 62, no. 10, pp. 6204–6212, Oct. 2015.

[13] J. F. Gieras, C. Wang, and J. C. Lai, *Noise of Polyphase Electric Motors*. New York, NY, USA: CRC Press, 2006.

[14] M. Valavi, A. Nysveen, R. Nilssen, R. D. Lorenz, and T. Rølvåg, "Influence of pole and slot combinations on magnetic forces and vibration in low-speed PM wind generators," *IEEE Trans. Magn.*, vol. 50, no. 5, May 2014, Art. no. 8700111.

[15] E. Carraro, N. Bianchi, S. Zhang, and M. Koch, "Design and performance comparison of fractional slot concentrated winding spoke type synchronous motors with different slot-pole combinations," *IEEE Trans. Ind Appl.*, vol. 54, no. 3, pp. 2276–2284, May/Jun. 2018.

[16] Z. Q. Zhu, Z. P. Xia, L. J. Wu, and G. W. Jewell, "Influence of slot and pole number combination on radial force and vibration modes in fractional slot PM brushless machines having single- and double-layer windings," in *Proc. IEEE Energy Convers. Congr. Expo.*, 2009, pp. 3443–3450.

[17] S. G. Min and B. Sarlioglu, "Investigation of electromagnetic noise on pole and slot number combinations with possible fractional-slot concentrated windings," in *Proc. IEEE Transp. Electrific. Conf. Expo.*, 2017, pp. 241–246.

[18] H. Fang, D. Li, R. Qu, and P. Yan, "Modulation effect of slotted structure on vibration response in electrical machines," *IEEE Trans. Ind. Electron.*, vol. 66, no. 4, pp. 2998–3007, Apr. 2019.

[19] H. Fang, D. Li, J. Guo, Y. Xu, and R. Qu, "Hybrid model for electromagnetic vibration synthesis of electrical machines considering tooth modulation and tangential effects," *IEEE Trans. Ind. Electron.*, vol. 68, no. 8, pp. 7284–7293, Aug. 2021.

[20] S. Zhu, W. Zhao, J. Ji, G. Liu, Y. Mao, and T. Liu, "Investigation of bread-loaf magnet on vibration performance in FSCW PMSM considering force modulation effect," *IEEE Trans. Transp. Electrific.*, vol. 7, no. 3, pp. 1379–1389, Sep. 2021.

[21] W. Liang, J. Wang, P. C. -K. Luk, and W. Fei, "Analytical study of stator tooth modulation on electromagnetic radial force in permanent magnet synchronous machines," *IEEE Trans. Ind. Electron.*, vol. 68, no. 12, pp. 11731–11739, Dec. 2021.

[22] H. Lan, J. Zou, Y. Xu, and M. Liu, "Effect of local tangential force on vibration performance in fractional-slot concentrated winding permanent magnet synchronous machines," *IEEE Trans. Energy Convers.*, vol. 34, no. 2, pp. 1082–1093, Jun. 2019.

[23] M. Liu, J. Zou, Y. Xu, H. Lan, and G. Yu, "Vibration enhancement or weakening effect caused by permanent magnet synchronous motor radial and tangential force formed by tooth harmonics," *Energies*, vol. 15, no. 3, pp. 744–754, Jan. 2022.

Jae-Hyun Kim received the Bachelor's degree in mechanical engineering in 2017 from Hanyang University, Seoul, South Korea, where he is currently working toward the Ph. D. degree in automotive engineering.

His research interests include the design, and the analysis of vibration and noise of electric machines.

Soo-Hwan Park received the Bachelor's degree in mechanical engineering in 2014 from Hanyang University, Seoul, South Korea, where he is currently working toward the Ph. D. degree in automotive engineering.

From 2019 to 2020, he was with the Korea Institute of Industrial Technology, Seoul, South Korea. His main research interests include electromagnetic field analysis, design and optimization of electric machines for automotive and robotics applications, and electric machine drive for industrial applications.

Jun-Yeol Ryu received the Bachelor's degree in mechanical engineering and electronic systems engineering from Hanyang University, Ansan, South Korea, in 2016. He is currently working toward the Ph. D degree in automotive engineering with Hanyang University, Seoul, South Korea.

His research interests include design and optimization of electric machines and analysis of electromagnetic field.

Myung-Seop Lim (Member, IEEE) received the Bachelor's degree in mechanical engineering in 2012, and the Master's and Ph.D. degrees in automotive engineering from Hanyang University, Seoul, South Korea, in 2012, 2014 and 2017, respectively.

From 2017 to 2018, he was a Research Engineer with Hyundai Mobis, Yongin, South Korea. From 2018 to 2019, he was an Assistance Professor with Yeungnam University, Daegu, South Korea, Since 2019, he has been with Hanyang University, Seoul, South Korea, where he is currently an Assistant Professor. His research interests include electromagnetic field analysis and electric machinery for mechatronics systems such as automotive and robot applications.